Mechanical perturbation control of cardiac alternans

Azzam Hazim,[1] Youssef Belhamadia,[2] and Stevan Dubljevic[3,*]

[1]*Department of Biomedical Engineering, University of Alberta, Edmonton, Alberta, Canada T6G 2V2*

[2]*Department of Mathematics and Statistics, American University of Sharjah, Sharjah, United Arab Emirates*

[3]*Department of Chemical and Materials Engineering, University of Alberta, Edmonton, Alberta, Canada T6G 2V4*

(Received 20 January 2017; published 21 May 2018)

Cardiac alternans is a disturbance in heart rhythm that is linked to the onset of lethal cardiac arrhythmias. Mechanical perturbation control has been recently used to suppress alternans in cardiac tissue of relevant size. In this control strategy, cardiac tissue mechanics are perturbed via active tension generated by the heart's electrical activity, which alters the tissue's electric wave profile through mechanoelectric coupling. We analyze the effects of mechanical perturbation on the dynamics of a map model that couples the membrane voltage and active tension systems at the cellular level. Therefore, a two-dimensional iterative map of the heart beat-to-beat dynamics is introduced, and a stability analysis of the system of coupled maps is performed in the presence of a mechanical perturbation algorithm. To this end, a bidirectional coupling between the membrane voltage and active tension systems in a single cardiac cell is provided, and a discrete form of the proposed control algorithm, that can be incorporated in the coupled maps, is derived. In addition, a realistic electromechanical model of cardiac tissue is employed to explore the feasibility of suppressing alternans at cellular and tissue levels. Electrical activity is represented in two detailed ionic models, the Luo-Rudy 1 and the Fox models, while two active contractile tension models, namely a smooth variant of the Nash-Panfilov model and the Niederer-Hunter-Smith model, are used to represent mechanical activity in the heart. The Mooney-Rivlin passive elasticity model is employed to describe passive mechanical behavior of the myocardium.

DOI: 10.1103/PhysRevE.97.052407

I. INTRODUCTION

Electrical alternans is a beat-to-beat long-short alternation in the cardiac action potential duration (APD) [Fig. 1(a)] [1], and is believed to be linked to the onset of lethal heart rhythm disorders such as ventricular fibrillation (VF) [2,3]. The diastolic interval (DI) (Fig. 1) is the time lapse between the end of the previous action potential and the next one (Fig. 1). It has been shown both clinically and experimentally that alternans degenerates quickly into ventricular tachycardia or fibrillation. Clinical manifestations of alternans is reflected in a beat-to-beat alternation of T-wave amplitude, known as T-wave alternans (TWA), on the electrocardiogram (ECG). The TWA is a marker of vulnerability to VF, and of sudden cardiac death (SCD) [4]. Experimentally, it has been observed that alternans can lead to complex spatiotemporal patterns along the epicardium and endocardium [5], and often precedes the development of more dangerous arrhythmias. Therefore, the suppression of cardiac alternans is potentially an effective strategy in preventing VF and SCD.

In the literature, electrical perturbation control has been the most studied approach to terminate alternans; see [6] for details. With this approach, the pacing cycle length (PCL) is perturbed by an amount proportional to the difference between the last two APDs. This control algorithm has been proven to be effective in controlling alternans in small tissues of up to 1 cm. A one-dimensional (1D) map that relates the DI at one beat to the APD of the subsequent beat via the restitution curve (see Sec. IV), is used to describe the alternans [7,8]. Another important factor influencing alternans is the bidirectional coupling between the membrane voltage (V) and intracellular calcium (Ca^{2+}) dynamics, where the APD alternans induces alternation in the amplitude of calcium transients through the $V \rightarrow Ca^{2+}$ coupling (Ca^{2+} alternans) (Fig. 1). Iterative maps [9–13] have been used to perform stability analysis of alternans. In [9], a two-dimensional (2D) discrete map at the single cell level is presented. At the tissue level, the amplitude of equations derived from the maps by taking into account the effect of electrotonic coupling is used to analyze the stability of the system of coupled maps [10]. Moreover, a theoretical framework of iterative maps describing the coupled dynamics of V and Ca^{2+} has been previously used at the subcellular and cellular levels [11–14].

Nearly all the work that has been done on the stability and control of alternans is electric based. However, recently a different approach for the suppression of alternans, based on the mechanical perturbation of cardiac tissue, was presented in [6,15]. This perturbation is reflected in cardiac excitation through the mechanisms of mechanoelectric feedback (MEF). The main advantage of this approach is that the alternans is suppressed in cardiac tissues of relevant size. In [6], we used a simple phenomenological model of cardiac excitation, while active tension was generated with an oversimplified isotropic active tension transient.

In this work, we analyze the effects of mechanical perturbation on the dynamics of the map-based model. This model is based on coupling between the membrane voltage and active

*Corresponding author: stevan.dubljevic@ualberta.ca

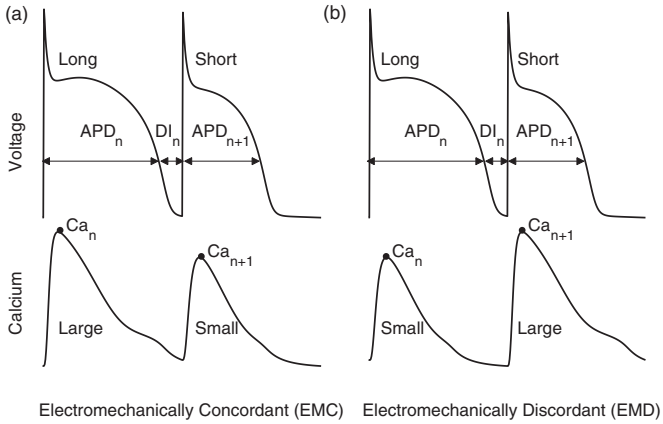

FIG. 1. Schematic representation of voltage and calcium alternans.

tension systems at the cellular level, and uses a theoretical framework of 2D iterative maps of the heart beat-to-beat dynamics. To make this possible, a simplified description of MEF is provided, and a coupled map model describing the bidirectional coupling between the membrane voltage and active tension at the cellular level is presented. Also, a discrete form of the proposed control algorithm that can be used in the coupled map model is derived. The stability of the model can be analyzed from the eigenvalues of a Jacobian matrix of the system of coupled maps.

In a second goal of this study, a biophysically detailed model of cardiac electromechanics is employed to investigate the control of alternans. We explore the feasibility of suppressing cardiac alternans in a realistic electromechanical model using the mechanical perturbation strategy. Luo-Rudy [16] and Fox [17] models are used to represent electrical activity in heart tissue, while mechanical properties are described by the Mooney-Rivlin material response [6,18]. Active tension that couples the electrophysiological model and the cardiac mechanics model is generated using a smooth variant of the Nash-Panfilov [19] model and the Niederer-Hunter-Smith [20] model. Numerical simulations are presented to demonstrate successful suppression of alternans in two realistic electromechanical models of cardiac tissue using the proposed control algorithm.

The paper is organized as follows. In Sec. II, we describe the cardiac electromechanical model used in this work. The mechanical perturbation control algorithm is presented in Sec. III. Section IV is devoted to theoretical analysis and a stability analysis of the derived system of coupled maps at the cellular level is provided. Section V presents numerical simulations demonstrating successful suppression of alternans by the proposed control algorithm, followed by a discussion. The findings are summarized in Sec. VI and future prospects are proposed.

II. CARDIAC ELECTROMECHANICAL MODEL

In this section, we describe mathematical equations that model the electrical excitation and mechanical contraction.

A. Cardiac mechanics

Mechanical analysis is based on the finite deformation elasticity theory, therefore a mathematical model of cardiac deformation is governed by equations of nonlinear elasticity. These equations are derived using Newton's laws of motion [6,18] and are expressed as

$$\frac{\partial}{\partial X_M}(S^{MN}F_{jN}) = 0, \tag{1}$$

where $F_{jN} = (\partial x_j/\partial X_M)$ is the deformation gradient tensor, X_M are the reference (undeformed) coordinates, x_i are the material (deformed) coordinates, the uppercase subscripts (M and N) and lowercase subscripts (i and j) correspond to the reference and current configurations, respectively, and S^{MN} is the second Piola-Kirchhoff stress tensor.

Two approaches, namely active strain and active stress, have been proposed to model the active mechanical response of the myocardium. For the active strain model, a multiplicative decomposition [21] of the deformation gradient tensor into a passive and an active part is assumed. The second model, which is the most widely used and it is adopted in this work, is based on the concept of active stress [18]. In this approach, S^{MN} is split into a passive and an active stress component [18], and is given by

$$S^{MN} = \frac{1}{2}\left(\frac{\partial W}{\partial C_{MN}} + \frac{\partial W}{\partial C_{NM}}\right) + T_a C^{-1}_{MN}, \tag{2}$$

where $W(I_1, I_2)$ is the strain energy function, $C_{MN} = (\partial x_k/\partial X_M)(\partial x_k/\partial X_N)$ is the right Cauchy-Green deformation tensor, and T_a is active tension generated by the electrical model. The isotropic Mooney-Rivlin constitutive model, which is used to describe passive mechanical properties of the cardiac tissue [6,18], is adopted in the present study, where the strain energy W is given by

$$W(I_1, I_2) = c_1(I_1 - 3) + c_2(I_2 - 3), \tag{3}$$

with $I_1(\boldsymbol{C}) = \mathrm{tr}(\boldsymbol{C})$ and $I_2(\boldsymbol{C}) = \frac{1}{2}[\mathrm{tr}(\boldsymbol{C}) - \mathrm{tr}(\boldsymbol{C}^2)]$ are the first two principal invariants of $\boldsymbol{C}$, and $\mathrm{tr}(\boldsymbol{C})$ is the trace of $\boldsymbol{C}$, and c_1 and c_2 are material constants.

The elastic equation (1) in one dimension can be written (see [6]) as

$$\tilde{c}\,\frac{\partial^2 u}{\partial X^2} + \frac{\partial}{\partial X}\left(\frac{T_a}{1 + \frac{\partial u(X)}{\partial X}}\right) = 0, \tag{4}$$

where $u = x - X$ is the displacement variable, x and X are material and reference coordinates respectively, and $\tilde{c} = 2(c_1 + 2c_2)$ is the material stiffness.

It has been shown in [22] that direct physiological influence of contraction on excitation of cardiac muscle cells, which is termed as mechanoelectric feedback, is given by depolarizing stretch-activated current (I_{sac}) through stretch-activated channels. I_{sac} can change the shape of the action potential in response to stretch. A linear voltage-current relationship has been found in experimental studies and linear ionic models have been proposed [23] for I_{sac}. In this work I_{sac} as described in [24] is adopted, and is given as

$$I_{sac} = G_s\frac{(\lambda - 1)}{(\lambda_{\max} - 1)}(V - E_s), \tag{5}$$

where G_s and E_s are maximal conductance and reversal potential, respectively, and λ is the extension ratio along the fiber direction, which is normalized by maximal stretch ($\lambda_{\max}$).

Following [24], the parameter G_s can take any value between 0 and 100 μS/μF, and E_s in most biophysical models takes the value of -20 mV. As shown in [24], cardiac cells are assumed to be stretched maximally between 5% and 10% of the resting position. The I_{sac} [Eq. (5)] is active during stretch, i.e., it is only present when $\lambda > 1$, otherwise, $I_{sac} = 0$, and is added to total ionic membrane current generated by the ionic model discussed under the cardiac excitation. In a 1D cable of heart tissue, we assume that cardiac fibers are parallel to the X direction of the undeformed body.

B. Cardiac excitation

A monodomain model is used to represent cardiac excitation, described by the following parabolic partial differential equation [25]:

$$C_m \frac{\partial V}{\partial t} = \frac{\partial}{\partial X_M}\left(D_{MN}\frac{\partial V}{\partial X_N}\right) - [I_{\text{ion}}(\mathbf{u}, V) + I_{\text{stim}}],$$
$$\frac{d\mathbf{u}}{dt} = \mathbf{f}(\mathbf{u}, V), \tag{6}$$

where V is the membrane voltage, D_{MN} is the diffusion tensor that accounts for electrical anisotropy of cardiac tissue, C_m is the membrane capacitance, I_{ion} is the ionic membrane current describing the excitable behavior of cardiac cells, $\mathbf{f}$ is a general function representing the choice of a cell model, $\mathbf{u}$ is the vector of dependent state variables containing ionic concentrations and membrane gating variables, and I_{stim} is the externally electrical stimulus applied at the pacing site. Two cardiac ionic models, namely, the Fox model given in [17] and the Luo-Rudy-1 (LR1) model [16], are employed in the present study to represent electrophysiological properties of the heart. LR1 is a mammalian ventricular cell based model which incorporates interaction between depolarization and repolarization and accounts for the calcium dynamics in cardiac myocyte. In total, the Luo-Rudy model consists of six individual currents, and of a system of eight ODEs including the intracellular calcium ion concentration. In 2002, Fox *et al.* [17] presented the canine ventricular myocyte, and it was the first model to ensure occurrence of alternans at fast pacing rates. This model uses 13 currents and consists of a system of 13 ODEs. Moreover, compared to the LR1 model, the Fox model incorporates a simplified description of intracellular calcium, therefore, it explicitly accounts for bidirectional coupling between the transmembrane potential and the intracellular Ca^{2+} concentration, while the LR1 model does not.

To take into account mechanical deformation of the tissue, neglected in this model, we modify Eq. (6) as described in [18,24] to obtain

$$C_m \frac{\partial V}{\partial t} = \frac{1}{\sqrt{C}}\frac{\partial}{\partial X_M}\left(\sqrt{C} D_{MN} C^{-1}_{MN}\frac{\partial V}{\partial X_N}\right) - [I_{\text{ion}}(\mathbf{u}, V) + I_{sac}(\lambda, V) + I_{\text{stim}}],$$
$$\frac{d\mathbf{u}}{dt} = \mathbf{f}(\mathbf{u}, V), \tag{7}$$

where $C = \det(C_{MN})$. A different approach, based on the concept of stress-assisted diffusion [26] to describe diffusion processes in a deforming excitable medium, such as cardiac tissue, is proposed. The diffusion tensors employed in [26] are directly influenced by the mechanical stress. Important effects of stress-assisted diffusion in the drifting and conduction velocity of excitation waves are revealed in their study.

C. Generation of active tension

In this study, two models of active tension, generated in response to electrical activation and coupled to nonlinear stress equilibrium equations, are considered.

The first model for the active tension generation is a smooth variant of the Nash-Panfilov (SVNP) model [18,19,27] which consists of one ODE and takes voltage as an input, and is given as follows:

$$\frac{\partial T_a}{\partial t} = \epsilon(V)\left[k_{T_a}(V - V_r) - T_a\right],$$
$$\epsilon(V) = \epsilon_0 + (\epsilon_\infty - \epsilon_0)\exp\{-\exp[-\xi(V - V_s)]\}, \tag{8}$$

where the parameter k_{T_a} controls the maximum value of T_a for a given potential V and a given resting potential V_r. $\epsilon(V)$ is the smoothly varying form for the switch function proposed in [18], given in terms of the parameters ϵ_0 and ϵ_∞ that represent the two limiting values of the function for $V < V_s$ and $V > V_s$ about the phase shift V_s, respectively, and the parameter ξ that determines the transition rate of ϵ from ϵ_0 to ϵ_∞ about V_s.

The second one is the Niederer-Hunter-Smith (NHS) model [20], which is an advanced model that depends on quantities derived from both the cardiac mechanics and excitation models. The NHS model consists of a system of five ODEs and the general form of the system can be written as

$$\frac{d\mathbf{w}}{dt} = \mathbf{g}\left(\mathbf{w}, \lambda, \frac{d\lambda}{dt}, [\text{Ca}^{2+}]_{\text{i}}, T_a\right),$$
$$T_a = h(\mathbf{w}), \tag{9}$$

where $\mathbf{w} = [w_1, w_2, w_3, w_4, w_5]$ is the vector of internal state variables for the contraction model, $\mathbf{g} = [g_1, g_2, g_3, g_4, g_5]$ and h are prescribed nonlinear functions. $[\text{Ca}^{2+}]_{\text{i}}$ is the intracellular concentration of Ca^{2+} ions generated by the ionic model, and λ is the extension ratio calculated from the mechanics model. The detailed form of equations for this model is given in [20]. In this model, cardiac contraction results from active tension generated by the myofilaments dynamics initiated by an increase in intracellular calcium concentration $[\text{Ca}^{2+}]_{\text{i}}$, where the concentration of calcium binds to troponin C (TnC), and follows tropomyosin kinetics with actin sites for myosin crossbridges. In this model, the Ca^{2+} binding to TnC is defined by

$$\frac{d[\text{Ca}^{2+}]_{\text{Trpn}}}{dt} = k_{\text{on}}[\text{Ca}^{2+}]_{\text{i}}([\text{Ca}^{2+}]_{\text{TrpnMax}} - [\text{Ca}^{2+}]_{\text{Trpn}}) - k_{\text{refoff}}\left(1 - \frac{T_a}{\Gamma\, T_{\text{ref}}}\right)[\text{Ca}^{2+}]_{\text{Trpn}}, \tag{10}$$

where k_{on} and k_{refoff} are the binding and unbinding rates of Ca^{2+} binding to TnC, $[\text{Ca}^{2+}]_{\text{Trpn}}$ is the concentration of Ca^{2+} bound to TnC, $[\text{Ca}^{2+}]_{\text{i}}$ is the cytosolic Ca^{2+} concentration, $[\text{Ca}^{2+}]_{\text{TrpnMax}}$ is the maximal concentration of Ca^{2+} that can bind to site (II), T_a is the active tension generated by the cell, and T_{ref} is the maximal isometric tension under zero strain while Γ is tension dependent buffering parameter. The values

of these parameters are given in [20]. Equation (10) can be written as

$$\frac{dw_1}{dt} = g_1\left(w_1,\lambda,\frac{d\lambda}{dt},[\mathrm{Ca}^{2+}]_\mathrm{i},T_a\right), \tag{11}$$

where $w_1 = [\mathrm{Ca}^{2+}]_\mathrm{Trpn}$, and $g_1(w_1,\lambda,\frac{d\lambda}{dt},[\mathrm{Ca}^{2+}]_\mathrm{i},T_a)$ is equal to the right-hand side of Eq. (10).

III. CONTROL ALGORITHM

Our control strategy is based on combining the spatially distributed mechanical perturbation algorithm [6] with the electrical boundary pacing algorithm [10] in order to control alternans. First, the tissue is paced at the boundary at PCL, named τ^*, such that the APD alternates. Under constant PCL, the amplitude of alternans [Eq. (26)] grows.

Boundary pacing control is realized by modulating the pacing interval based on the consecutive APDs at the pacing site, and is determined by the dynamic control scheme [10]:

$$T^n = \tau^* + \gamma\,[\mathrm{APD}_n(\zeta=0) - \mathrm{APD}_{n-1}(\zeta=0)]. \tag{12}$$

T^n represents the amount of time between the $(n-1)$th and nth stimuli, and ζ represents space. Here γ is the feedback gain. As described in [6], this feedback control has the effect of lengthening or shortening T^n at the nth stimulus based on the difference of two consecutive APDs. This approach is capable of suppressing cardiac alternans at the pacing site and up to a finite distance ($\leqslant 1$ cm) [10,28,29]. Beyond that region, the instabilities grow along the tissue. To overcome this limitation in controllability, we combined it with a spatially distributed mechanical perturbation algorithm [6].

Depending on the active tension mathematical model employed, two different mathematical implementations are used to implement the mechanical perturbation control strategy.

For the SVNP model, the spatially distributed mechanical perturbation control algorithm is implemented as follows:

$$\frac{\partial T_a}{\partial t} = \epsilon(V)\left[k_{T_a}(V-V_r) - T_a\right] + \beta e_n(\zeta),$$
$$e_n(\zeta) = \begin{cases} \mathrm{APD}_\mathrm{ref}(\tau^*) - \mathrm{APD}_{n-1}(\zeta), & \text{if } \rho > 0 \\ 0, & \text{if } \rho \leqslant 0 \end{cases}, \tag{13}$$

where β is the controller gain, and $\rho = \mathrm{APD}_\mathrm{ref}(\tau^*) - \mathrm{APD}_{n-1}(\zeta)$. The error $e_n(\zeta)$ is generated from the difference between APD references $[\mathrm{APD}_\mathrm{ref}(\tau^*)]$ recorded between the time we reach τ^* and the following beat, over the local area under control, and the APDs at the $(n-1)$th stimulus (APD_{n-1}), over the same area length. This means that the mechanical properties of cardiac tissue are perturbed as a result of T_a perturbation [an additional term given by $\beta e_n(\xi)$ is added into T_a] when $e_n(\xi)$ is not null. The reader can refer to [6] for more details.

This basic feedback algorithm takes $e_n(\zeta)$ and provides a control signal which is applied over the region under control. The control signal is not null only when $e_n(\zeta) > 0$, meaning that the controller only acts on the short APD. It is added as a positive quantity to Eq. (13), when the transmembrane potential crosses the threshold value, named V_{th}, during the repolarization phase at the nth stimulus until the resting potential V_r. In the control algorithm, V_{th} is set to E_s, the reversal potential defined in Eq. (5). Therefore we can assume that I_{sac} has the same sign (inward current) when control is activated. The controller acts after the electrical boundary feedback controller stabilizes a finite part of the tissue length ($\approx$1 cm).

For the NHS model, the spatially distributed mechanical perturbation control algorithm is implemented as follows:

$$\frac{dw_1}{dt} = g_1\left(w_1,\lambda,\frac{d\lambda}{dt},[\mathrm{Ca}^{2+}]_\mathrm{i},T_a\right) + \beta_1 e_{1n}(\zeta),$$
$$e_{1n}(\zeta) = \begin{cases} \mathrm{APD}_\mathrm{ref}(\tau^*) - \mathrm{APD}_{n-1}(\zeta), & \text{if } \rho > 0 \\ 0, & \text{if } \rho \leqslant 0 \end{cases}, \tag{14}$$

where β_1 is the controller gain, and $\rho = \mathrm{APD}_\mathrm{ref}(\tau^*) - \mathrm{APD}_{n-1}(\zeta)$. The functionality of $e_{1n}(\zeta)$ is the same as $e_n(\zeta)$. Also, in this model the controller acts after the electrical boundary feedback controller stabilizes approximately 1 cm of the tissue length.

IV. THEORETICAL ANALYSIS

In this section, we analyze the effects of the mechanical perturbation algorithm on the dynamics of the map model that couples the membrane voltage and active tension systems at the cell level. Therefore, we introduce a 2D iterative map of the beat-to-beat dynamics, and a discrete form of the proposed control algorithm that can be incorporated in the coupled map model is derived. Then, we perform stability analysis of the system of the coupled maps. This analysis is performed using the SVNP model, which describes qualitatively consistent timing and amplitude of cardiac tissue contraction [30]. While the active cell tension is better represented using the NHS model that accurately describes the relationship between the intracellular calcium transient and tension, the selection of the SVNP model is made due to the simplicity of the governing equations of this model, where a discrete form of the control algorithm can be derived. In addition, in this study, we are investigating the effects of mechanical perturbation (stretch-based control algorithm) on alternans to gain insight into the effectiveness of the control algorithm, that have been confirmed by numerical experiments, using both SVNP and NHS models of active tension. While these two models do not generate the same quantitative results (shape and magnitude) of I_{sac}, which causes either the lengthening or shortening of the action potential as discussed in the next section, qualitatively similar results of I_{sac} (approximately proportional increases or decreases of I_{sac} from beat to beat) are obtained for both models.

A. Map model development

The electrophysiology of a cell experiences feedback from tissue deformation, which activates stretch sensitive ion channels, is described in Sec. II. Therefore, I_{sac} [Eq. (5)], which is a function of two variables λ [Eq. (5)] and V [Eq. (7)], should be expressed only in terms of V and T_a [Eq. (8)], to have direct coupling between voltage and active tension. To this end, an approximation of λ in terms of T_a is given in Appendix A. Thus, λ as given in Eq. (A7) is a function of T_a only, and the simplified description of I_{sac}, after replacing the approximate value of λ

TABLE I. Parameter values used in SVNP model.

Active tension	$k_{T_a} = 0.34 \times 10^{-3}$ MPa mV^{-1}
Switch function	$\epsilon_0 = 1$ ms^{-1}, $\epsilon_\infty = 0.1$ ms^{-1}, $\xi = 0.3$ mV^{-1}, $V_s = -70$ mV

in Eq. (5), becomes a function of V and T_a. Therefore, the simplified fully coupled electromechanical cell (CEC) model is constituted by Eqs. (7), (8), (5), and (A7).

In the following, we check the effectiveness of mechanical and electrical perturbation controls in suppressing the alternans using the simplified CEC model. For numerical demonstration, a 1D cardiac cable of length $L = 1$ cm and fixed at end points is considered. The step sizes and parameters of this model are given in Sec. V and in Tables I and II. The APD alternans is induced by pacing the cable in the middle with PCL $= 200$ ms until steady state is reached. Electrical perturbation control is given in Eq. (12) with $\gamma = 0.15$, and mechanical perturbation control is given in Eq. (13), and $e_n(\zeta)$ takes the form given by Eq. (65) in [15], and therefore we obtain

$$\frac{\partial T_a}{\partial t} = \epsilon(V)\big(k_{T_a}(V - V_r) - T_a\big) + \beta e_n(\zeta),$$
$$e_n(\zeta) = \begin{cases} \mathrm{APD}_n(\zeta) - \mathrm{APD}_{n-1}(\zeta), & \text{if } \rho < 0 \\ 0, & \text{if } \rho \leqslant 0 \end{cases}, \quad (15)$$

where $\epsilon(V)$ is defined in Eq. (8). The values of original parameters of $\epsilon(V)$, given in [19], are modified (see Table I), in order to take into account time delay as illustrated in Fig. 2(a) in [18]. The controller gain β is chosen to be -0.002. Therefore, in both control algorithms (electrical and mechanical), we have the same error signal which is generated by the difference between two consecutive APDs. In the case of electrical control, the pacing interval is being perturbed, while in the case of mechanical control, we are perturbing T_a. As shown in Fig. 2, the alternans is suppressed (no alternation in the APD at steady state), when control (electrical or mechanical) is activated. While both control algorithms have successfully suppressed alternans at a single cardiac cell, their effectiveness at the tissue level is not equal, since, among other things, a spatially extended electrical perturbation algorithm for controlling alternans is not feasible; see [6] for details.

The second step in this development is to introduce a 2D discrete map describing the coupled dynamics of the membrane voltage and the active tension. The APD alternans can be mathematically described using the following discrete map:

$$\mathrm{APD}_n = F(\mathrm{DI}_{n-1}). \quad (16)$$

The relation in Eq. (16), known as APD restitution, relates APD at beat n with DI at beat $n-1$. It dictates that a shortened (prolonged) DI at a given beat will be followed by a shortened

TABLE II. Values of the material parameters used for the models.

Stretched-activated current	$G_s = 10\ \mu$S μF^{-1}, $E_s = -20$ mV, $\lambda_{\max} = 1.1$
Mooney-Rivlin	$\tilde{c} = 0.4$ MPa

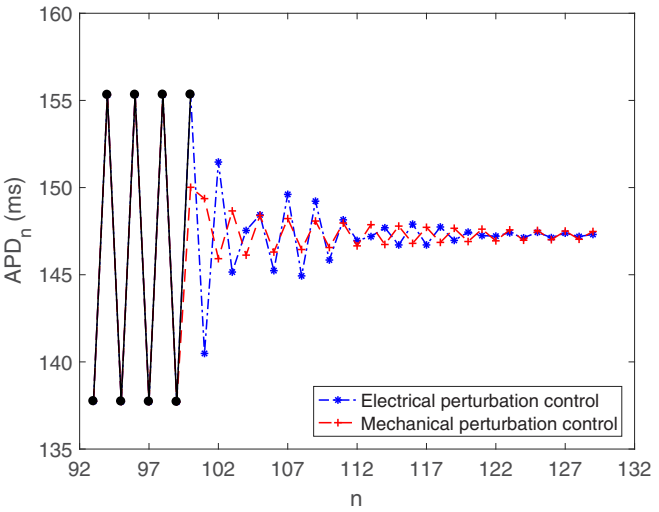

FIG. 2. Evolution of the APD vs the beat number (n) of a single cardiac cell in the middle of the cable of length $L = 1$ cm, when it is paced at the center with PCL $= 200$ ms until steady state is reached (black line), using the CEC model [Eqs. (7), (8), (5), and (A7)] where FOX model is used to represent electrical activity, with parameters given in Sec. V and in Tables I and II. Evolution of APD vs n, when mechanical perturbation control (red dashed line), or electrical perturbation control (blue dash-dot line), applied at beat 100, are obtained using the CEC model except that Eq. (15) (with $\beta = -0.002$) is used instead of Eq. (8) for the case of mechanical control, and Eq. (12) (with $\gamma = 0.15$) is added to the CEC model for the case of electrical control.

(prolonged) APD at the next beat. The interval T^n [Eq. (12)] can be written as $T^n = \mathrm{APD}_n + \mathrm{DI}_n$. At a constant PCL, where $T^n = \tau$ for all n, prolonging a given APD will shorten the following DI, and therefore the next APD is shortened. APD restitution is usually measured using an S1S2 pacing protocol. In the S1S2 protocol, the cell is paced at a fixed cycle length S1 until steady state is reached, and then a premature S2 stimulus is applied to elicit an extra beat. This S1S2 stimulus train is repeated and the S2 intervals are shortened each time until conduction block occurs. Theoretical studies have indicated that the periodic fixed point of Eq. (16) corresponding to the stable 1:1 rhythm undergoes a period-doubling bifurcation (2:2 rhythm), leading to the APD alternation, when the slope of the APD restitution curve is greater than 1. It has to be noted that in large tissues, while most of the tissue may follow a 2:2 response, some regions can develop into higher-order rhythms such as 4:4 and 8:8 during fast pacing [5]. However, several experimental results have shown that this hypothesis (slope $>$ 1) fails to predict the onset of alternans when other factors, such as calcium cycling, have a strong influence on action potential. Therefore, in [12,13], a 2D iterative map is used to explore the effects of coupling between voltage and intracellular calcium transients, and is given by

$$\mathrm{APD}_n = Fc_1(\mathrm{APD}_{n-1}, \mathrm{Ca}_n),$$
$$\mathrm{Ca}_n = Fc_2(\mathrm{APD}_{n-1}, \mathrm{Ca}_{n-1}), \quad (17)$$

which relates the APD_n at a given beat to the APD_{n-1} at previous beat, due to the APD restitution [Eq. (16)], and the peak Ca_n (Fig. 1) of the same beat, due to the effects of

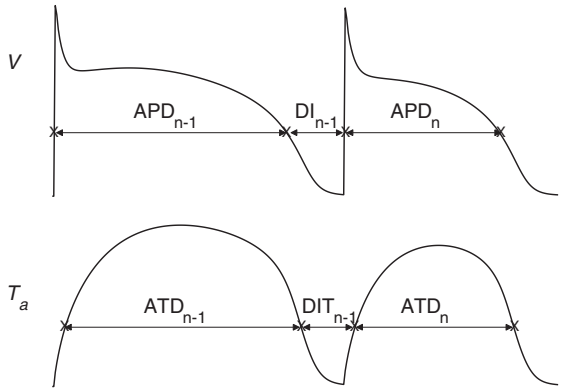

FIG. 3. Schematic representation of membrane voltage and active tension, illustrating the APD and the ADT, using the CEC model where Fox model is used to represent the electrical activity, in the presence of alternans.

calcium-sensitive membrane currents, and relates the Ca_n at a given beat to the APD_{n-1} and the peak Ca_{n-1} at the previous one. The Ca^{2+} modulates membrane currents through the $Ca^{2+} \rightarrow V$ coupling, affecting the APD, and as dictated in Eq. (17), the coupling from Ca^{2+} to V occurs during the concurrent beat. The situation where APD and Ca^{2+} alternans are in phase, the case where long and short APD correspond to large and small Ca^{2+} respectively, is referred to as electromechanically concordant (EMC) alternans [12] [Fig. 1(a)]. The opposite situation is known as electromechanically discordant (EMD) alternans [Fig. 1(b)].

To take into account the effects of MEF, and based on numerical experiments of the CEC model [Eqs. (7), (8), (5), and (A7)] where the Fox model is used to represent electrical activity, with parameters given in Sec. V and in Tables I and II, we use a semi-implicit formulation of 2D maps that relates the APD and the active tension duration (ATD) (Fig. 3), and is given by

$$\begin{aligned} \mathrm{APD}_n &= F_1(\mathrm{APD}_{n-1}, \mathrm{ATD}_n), \\ \mathrm{ATD}_n &= F_2(\mathrm{APD}_{n-1}, \mathrm{ATD}_{n-1}), \end{aligned} \tag{18}$$

where ATD_n (lower part of Fig. 3) is the T_a width at beat n, measured from the instant when T_a crosses the threshold value on the wave front, until the instant it falls below the threshold value on the wave back, and APD_n (upper part of Fig. 3) is the V width at beat n, measured from the instant when V crosses the threshold value on the wave front, until the instant it falls below the threshold value on the wave back. Similarly to the APD in Eq. (17), the APD of the current beat (APD_n) [Eq. (18)] is a function of both the previous APD (APD_{n-1}) and the concurrent ATD (ATD_n), due to the effects of I_{sac} that changes the repolarization of membrane voltage. Also in this model, the coupling from active tension to voltage ($T_a \rightarrow V$ coupling) occurs during the concurrent beat. Note that the 2D map [Eq. (18)] is also valid when the NHS model is used, but the width of T_a (ATD_n) at beat n needs to be replaced by the T_a transient peak (ATP_n).

B. Discrete form of the control algorithm

A discrete form of mechanical perturbation control algorithm that can be incorporated in the 2D maps [Eq. (18)] is derived in the following manner.

To compute the current value of T_a at a single point in space, we discretize Eq. (8) in time k using an explicit forward Euler scheme. The closed-form expression for T_a reads

$$\begin{aligned} T_a^k &= T_a^{k-1} + \Delta t\ \epsilon(V^{k-1}) \left[k_{T_a}(V^{k-1} - V_r) - T_a^{k-1}\right], \\ \epsilon(V^{k-1}) &= \epsilon_0 + (\epsilon_\infty - \epsilon_0)\ \{-\exp[-\xi(V^{k-1} - V_s)]\}. \end{aligned} \tag{19}$$

When control is activated, the current value of active tension, named T_a^{pert}, is perturbed, by adding the term $\Delta t\ \beta\ e_n$ [$e_n = \mathrm{APD}_{\mathrm{ref}}(\tau^*) - \mathrm{APD}_{n-1}$, Eq. (13)], into the right-hand side of Eq. (19), and therefore, at beat n, we can equivalently write

$$\mathrm{ATD}_n^{\mathrm{pert}} = \mathrm{ATD}_n + \alpha\ [\mathrm{APD}_{\mathrm{ref}}(\tau^*) - \mathrm{APD}_{n-1}], \tag{20}$$

where $\mathrm{ATD}_n^{\mathrm{pert}}$ is the width of T_a^{pert} at beat n, and α is a parameter that depends on β. Note that the discrete form of T_a [Eq. (20)], expressed in its ATD form, states that the control signal is delivered in a given beat when control is activated. On the other hand, continuous-time control law is implemented [Eq. (13)], which means it is defined over a continuous time interval in a given beat.

C. Stability analysis

In this section, we present linear stability analysis of the 2D iterative maps describing the coupled dynamics of voltage and active tension and incorporating mechanical perturbation control derived in its discrete form. The system's behavior of the open-loop or controlled coupled maps, close to the alternans bifurcation, can be accessed from the eigenvalues of the Jacobian matrix of the system. First, we linearize the system [Eq. (18)] around the period-1 fixed point (APD_*,ATD_*) by letting $\mathrm{APD}_{n-1} = \mathrm{APD}_* + \delta\mathrm{APD}_{n-1}$ and $\mathrm{ATD}_{n-1} = \mathrm{ATD}_* + \delta\mathrm{ATD}_{n-1}$, see Appendix B, and we obtain

$$\delta X_n \approx J\ \delta X_{n-1}, \tag{21}$$

where $\delta X_n = [\delta\mathrm{APD}_n, \delta\mathrm{ATD}_n]^T$, and J is the Jacobian of the two-variable map evaluated at the fixed point (APD_*,ATD_*), and is given by

$$J = \begin{pmatrix} \frac{\partial \mathrm{APD}_n}{\partial \mathrm{APD}_{n-1}} + \frac{\partial \mathrm{APD}_n}{\partial \mathrm{ATD}_n}\frac{\partial \mathrm{ATD}_n}{\partial \mathrm{APD}_{n-1}} & \frac{\partial \mathrm{APD}_n}{\partial \mathrm{ATD}_n}\frac{\partial \mathrm{ATD}_n}{\partial \mathrm{ATD}_{n-1}} \\ \frac{\partial \mathrm{ATD}_n}{\partial \mathrm{APD}_{n-1}} & \frac{\partial \mathrm{ATD}_n}{\partial \mathrm{ATD}_{n-1}} \end{pmatrix}, \tag{22}$$

which describes the system's behavior around its fixed point (APD_*,ATD_*). The signs of the elements of J play an important role in the stability of J, hence, descriptions of all the terms of the Jacobian matrix for the case of CEC model are given below. In all numerical experiments, we assume voltage-driven alternans in which APD alternans is caused by instabilities originating from voltage, and that the width variations of V and T_a occur when V crosses E_s, since control is activated only when V crosses E_s. If only voltage is coupled to tension (one way coupling), it is the case of a cardiac electromechanical model when MEF is neglected ($I_{sac} = 0$); $-J_{11}$ simply measures the slope of the APD restitution relation [Eq. (16)], since when $I_{sac} = 0$, we have $\partial\mathrm{APD}_n/\partial\mathrm{ATD}_n = 0$, and consequently $J_{11} = \partial\mathrm{APD}_n/\partial\mathrm{APD}_{n-1} = -\partial\mathrm{APD}_n/\partial\mathrm{DI}_{n-1}$. When

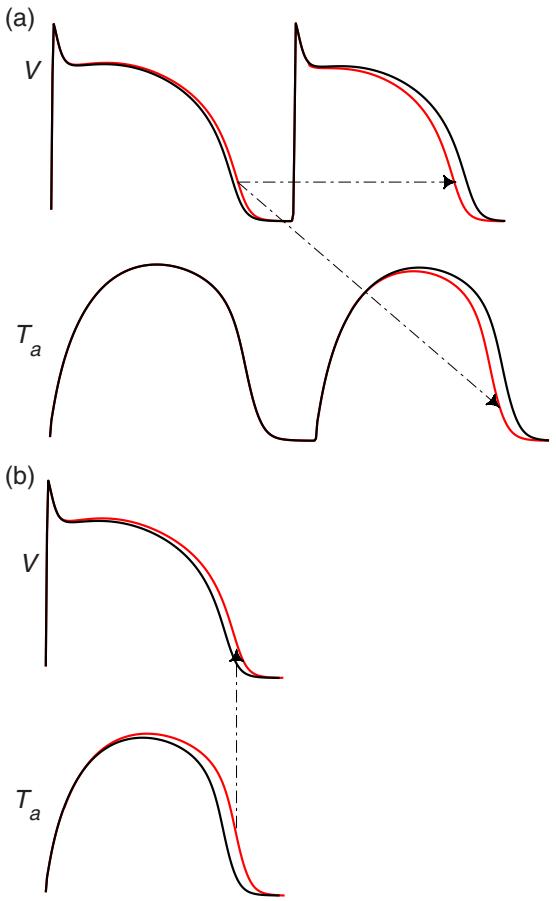

FIG. 4. (a) Illustration of APD restitution relation and graded release coupling in CEC model. An increase in the APD (red line) at a given beat leads to a decrease in the APD (red line) and ATD (red line) at the next beat (due to a shortening of the DI), and vice versa. (b) Illustration of $T_a \rightarrow V$ coupling in CEC model. An increase in the ATD (red line) at a given beat tends to prolong the APD (red line) of that beat (due to the effects of I_{sac}). Fox model is used to represent the electrical activity in CEC model.

the slope is larger than unity, which corresponds here to the condition $J_{11} < -1$, APD alternans occurs and induces ATD alternans; see also the discussion in Sec. V. In turn, J_{22} measures the degree of instability of the tension system in the CEC model, and is negative but greater than -1, since in our case ATD alternans is secondary to APD alternans. The term $\partial \mathrm{APD}_n/\partial \mathrm{ATD}_n$ measures dependence of the voltage on the tension, and is positive in the CEC model [Fig. 4(b)]. This is equivalent to the so called positive ($T_a \rightarrow V$ coupling), which states that a prolongation (shortening) in ATD will prolong (shorten) concurrent APD, and means that an increase (decrease) in ATD has a net depolarizing (hyperpolarizing) effect on voltage. Since $\partial \mathrm{ATD}_n/\partial \mathrm{ATD}_{n-1} = J_{22}$ is negative and $\partial \mathrm{APD}_n/\partial \mathrm{ATD}_n$ is positive, one can conclude that $J_{12} = (\partial \mathrm{APD}_n/\partial \mathrm{ATD}_n)(\partial \mathrm{ATD}_n/\partial \mathrm{ATD}_{n-1})$ is negative. The term $\partial \mathrm{ATD}_n/\partial \mathrm{APD}_{n-1} = J_{21}$ measures the dependence of each beat's ATD on the preceding APD ($V \rightarrow T_a$ coupling), called graded release, and is negative in the CEC model [Fig. 4(a)]. It states that a prolongation of the preceding APD (APD_{n-1}) will cause a shortening in the subsequent ATD (ATD_n), and vice versa.

The stability of the system of coupled maps [Eq. (18)] is governed by the eigenvalues of the Jacobian matrix. The eigenvalues of the matrix J are given by

$$\lambda_1 = \tfrac{1}{2}(J_{11} + J_{22} + \sqrt{(J_{11} - J_{22})^2 + 4J_{12}J_{21}}),$$
$$\lambda_2 = \tfrac{1}{2}(J_{11} + J_{22} - \sqrt{(J_{11} - J_{22})^2 + 4J_{12}J_{21}}). \quad (23)$$

The period-1 fixed point is stable provided that the absolute value of the largest eigenvalue of J, which is λ_2, is smaller than 1. If $\lambda_2 < -1$, the fixed point goes unstable and a period-doubling bifurcation occurs, corresponding to the onset of alternans.

To analyze the effect of the mechanical perturbation control on the system of coupled maps, we model the effects of mechanical control on the elements of J [Eq. (22)], by incorporating its discrete form [Eq. (20)] in J. The new Jacobian matrix called J^c is given as

$$J^c = \begin{pmatrix} J_{11} - \alpha \frac{\partial \mathrm{APD}_n}{\partial \mathrm{ATD}_n} & J_{12} \\ J_{21} - \alpha & J_{22} \end{pmatrix}, \quad (24)$$

where α is not null when control is activated, otherwise it is set to zero. Mechanical perturbation control will thus affect two elements in J^c ($J^c_{11} = J_{11} - \alpha\ (\partial \mathrm{APD}_n/\partial \mathrm{ATD}_n)$ and $J^c_{21} = J_{21} - \alpha$). Therefore, we analyze the effect of these two elements on the stability of the system. Let us assume that at the beat n the control is activated; the APD dynamics manifested by $\partial \mathrm{APD}_n/\partial \mathrm{APD}_{n-1}$ can be stabilized with negative α, since $\partial \mathrm{APD}_n/\partial \mathrm{ATD}_n$ is positive (discussed above). Likewise, the $V \rightarrow T_a$ coupling manifested by $\partial \mathrm{ATD}_n/\partial \mathrm{APD}_{n-1}$ will become weaker with negative α and $\partial \mathrm{ATD}_n/\partial \mathrm{APD}_{n-1} - \alpha$ remains negative. We can illustrate this by calculating the eigenvalues of J^c, which are given by

$$\lambda^c_1 = \tfrac{1}{2}\left(J^c_{11} + J_{22} + \sqrt{\left(J^c_{11} - J_{22}\right)^2 + 4J_{12}J^c_{21}}\right),$$
$$\lambda^c_2 = \tfrac{1}{2}\left(J^c_{11} + J_{22} - \sqrt{\left(J^c_{11} - J_{22}\right)^2 + 4J_{12}J^c_{21}}\right), \quad (25)$$

where (J_{12}, J_{22}) are elements of J [they are used in Eq. (25), since they do not depend on α]. For certain values of α, as shown in Fig. 5, the absolute value of the largest eigenvalue is smaller than 1. The properties of the 2D discrete maps determine the range of α, and consequently the controller gain β [defined in Eq. (13)], which provides effective control. As demonstrated above, the mechanical perturbation control is effective in controlling alternans at the cellular level. In the next section, the suppression of alternans at the tissue level will be numerically demonstrated.

V. NUMERICAL RESULTS AND DISCUSSION

We have simulated the control algorithms and successfully suppressed alternans using either SVNP or NHS models for the active tension generation with either Fox or LR1 models for the cardiac excitation described in Sec. II. Therefore, for brevity, only numerical simulations obtained with NHS model and with either Fox or LR1 models are presented and discussed in this section. The NHS model is chosen since the

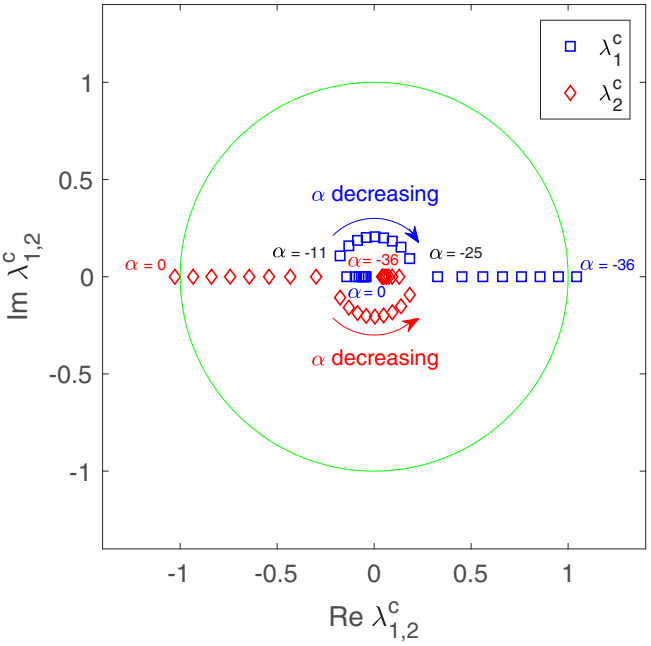

FIG. 5. Diagram of the two eigenvalues (the imaginary and real parts of $\lambda^c_{1,2}$) of the Jacobian matrix J^c for various values of α. $\lambda^c_{1,2}$ (marked by blue squares and red lozenges) are calculated using the CEC model [Eqs. (7), (8), (5), and (A7)] where Fox model is used to represent the electrical activity, with parameters given in Sec. V and in Tables I and II. The 1D tissue is paced at the center with PCL = 207 ms, and the terms that constitute the elements of J are evaluated at the period-1 fixed point. For $\alpha = 0$ (no control is applied), the absolute value of the largest eigenvalue of J^c ($|\lambda^c_2|$), which is a measure of the stability of the fixed point, is greater than 1. When $\alpha < 0$, the absolute value of λ^c_2 is decreased and λ^c_1 is increased. For $\alpha <= -36$, λ^c_1, which becomes the largest eigenvalue of J^c when $\alpha < -25$, is greater than 1. Both eigenvalues become complex when $\alpha < -11$ and $\alpha > -25$.

relationship between Ca^{2+} and T_a is more accurately described in this model. Thus, Eqs. (4), (5), (7), and (9) are used to constitute the two electromechanical models in this section. In all our simulations, a 1D cardiac cable of length $L = 6.25$ cm, fixed at end points, is considered, which is consistent with an isometric contraction regime. In one dimension, the upper case indices (M,N) presented in Eq. (7) are set to 1, $D_{11} = \bar{D} = 0.001$ cm^2/ms is the diffusion constant, and $C_m = 1$ μF/cm^2 is the membrane capacitance. The electrical stimulus is applied as square wave pulses with a magnitude of 80 μA/μF and a duration of 1 ms. The same numerical schemes were applied in all simulations, where Eq. (7) was solved by a semi-implicit time integration scheme, and the Hodgkin-Huxley type equations for the gating variables in the ionic models (LR1, Fox) were integrated using the Rush and Larsen integration scheme [31]. The active tension generation [Eq. (9)] was solved using the standard Euler scheme, and we determined the tissue deformation mechanics [Eq. (4)] using the finite difference scheme. The step time $\Delta t = 0.005$ ms and step size $\Delta X = 0.0125$ cm are used in all simulations, and no-flux boundary conditions were imposed for Eq. (7). The parameters for all models, including cardiac mechanics, used in the simulation are given in Table II.

A. Model 1: Using LR1 and NHS models

In the first electromechanical model, LR1 and NHS models are used to represent electrophysiological properties and active tension generation respectively. The LR1 [16] model, where the resting potential is about $V_r = -83.4$ mV, is used with modifications of the maximum conductances of the sodium current ($\bar{G}_{Na} = 16.0$ instead of 23.0), of the slow inward current ($\bar{G}_{si} = 0.06$ instead of 0.09), and of the time-dependent potassium current ($\bar{G}_K = 0.432$ instead of 0.282), so that the model is capable of showing alternans at a shorter cycle length. In this model, the gains $\gamma = 0.23$, $\beta_1 = -4.2 \times 10^{-4}$ are chosen.

The amplitude of alternans, $a_n(\zeta)$, is defined as the difference between two consecutive APDs at a given point in space ζ:

$$a_n(\zeta) = [\mathrm{APD}_n(\zeta) - \mathrm{APD}_{n-1}(\zeta)](-1)^n. \tag{26}$$

To induce alternans, we pace the first ten cells of the cable, located at one end from the pacing site ($\boldsymbol{P}$), at $\tau = 300$ ms, until a steady-state APD is reached, and gradually decreased τ from 300 to $\tau^* = 255$ ms. The pacing period was shortened in steps of 5 ms for $\tau > 260$ ms and in steps of 1 ms for $\tau < 260$ ms. When pacing with period $\tau^* = 255$ ms, the alternans [Fig. 6(a)] grows, and when the control action is applied at $t = 33\,000$ ms, over localized region under control (3.25–5 cm), it successfully suppresses alternans [Fig. 6(c)]. The controller acts after the electrical boundary feedback controller stabilizes the area up to 1 cm from $\boldsymbol{P}$ [Fig. 6(b)]. As seen in this figure, the electrical pacing control cannot achieve stability for the cables exceeding 1 cm, hence the need for a model-based control algorithm that combines the boundary pacing with the spatially distributed mechanical perturbation. As shown in Fig. 7, APDs alternate in a repeating long-short pattern when control is not applied [Fig. 7(a)] and are restored (normal APDs), in the area up to 1 cm from $\boldsymbol{P}$ [Fig. 7(b)], after the electrical control is applied at $\boldsymbol{P}$, and along the cable when both the electrical and mechanical perturbation controls are applied [Fig. 7(c)].

After applying the spatially distributed mechanical perturbation control at $t = 33\,000$ ms, the largest changes in I_{sac} [Fig. 8(b)] with respect to I_{sac}, when only the electrical boundary pacing control is applied [Fig. 8(a)], occur in the localized region (3.25–5 cm) where the control signal is applied. The mechanical perturbation control perturbs the tissue by exerting a force that causes deformation in the region under control, and as a result, the stretch distribution along the tissue changes, it increases in the region under control, and decreases in other regions. This is because, since the sum of the length of all the line segments, when stretched (increased) or contracted (decreased), of the 1D cable, remains constant when both ends of the cable are fixed, see Appendix A, some segments are stretched, while others are contracted. Consequently, the magnitude of I_{sac}, which is a function of stretch and voltage [Eq. (5)], when mechanical perturbation control is applied, increases in the localized region under control (3.25–5 cm from $\boldsymbol{P}$), and decreases elsewhere. As can be seen in Fig. 8(d), the short APDs during one beat [the odd beats in Fig. 8(d)], in the area under control, are prolonged due to the I_{sac}, which causes, according to the restitution relation [Eq. (16)], the shortening of APDs on the following beat [the even beats in

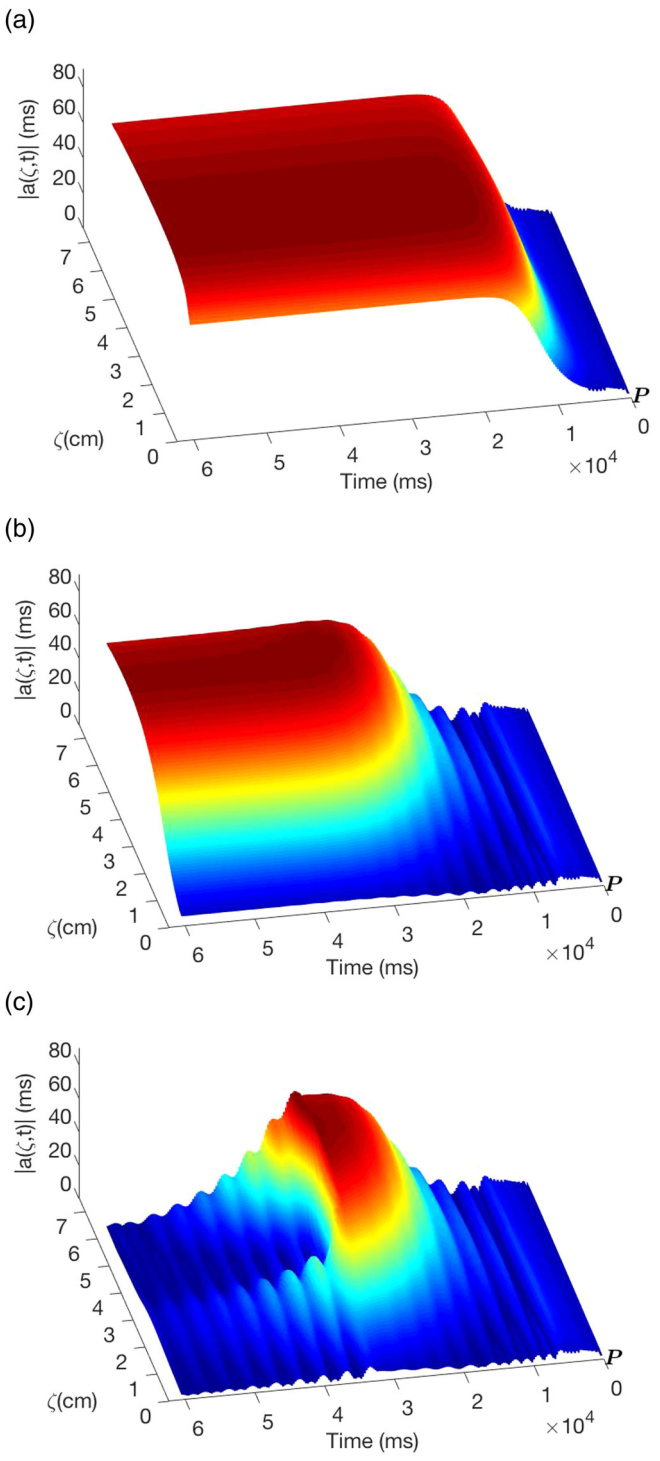

FIG. 6. Magnitude of the amplitude of alternans for model 1 when a 6.25-cm cable of cardiac cells, the first ten cells to pacing site $\boldsymbol{P}$ (which corresponds to $\zeta = 0$), is paced at 255 ms, starting with period =300 ms, and decreased gradually to period =255 ms. The amplitude of alternans grows, shown in (a), when no control is applied, while (b) illustrates the alternans suppression by electrical pacing control applied at $\boldsymbol{P}$ when $\tau^* = 255$ ms is reached, and (c) illustrates the alternans suppression by electrical pacing control and spatially distributed mechanical perturbation control when the control action is applied at $t = 33\,000$ ms over localized region under control (3.25–5 cm from $\boldsymbol{P}$).

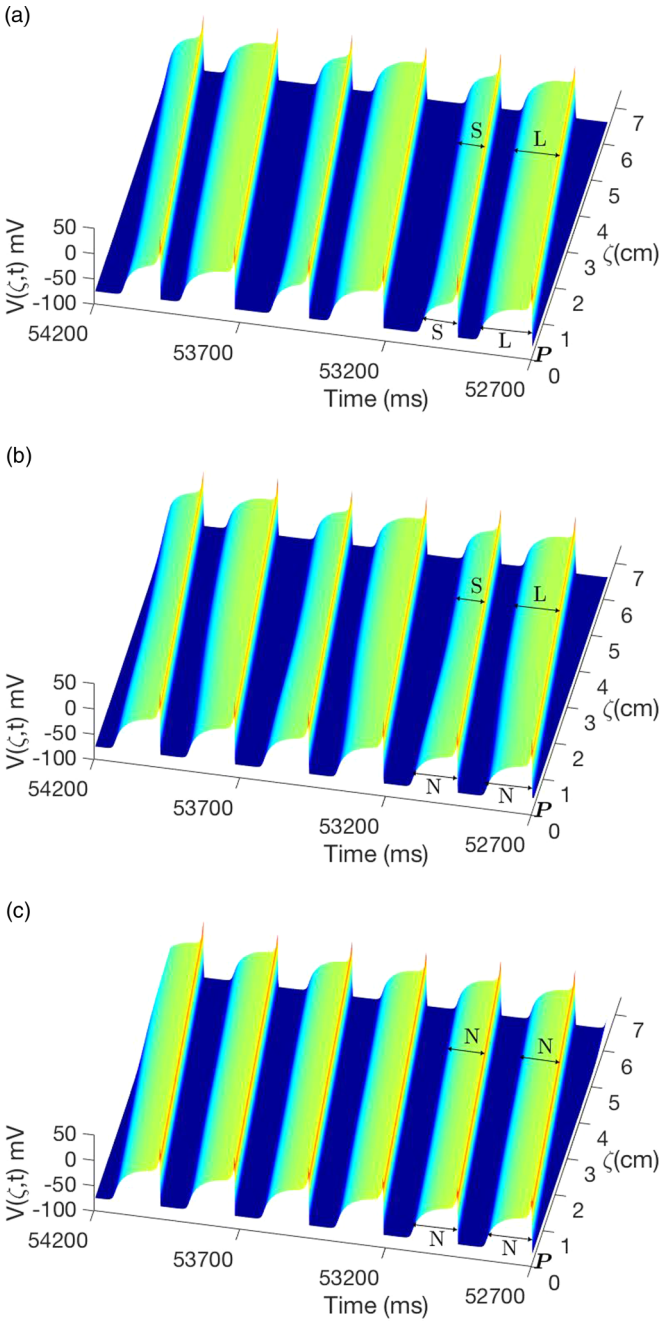

FIG. 7. Time evolution of transmembrane potential for model 1 before control is applied (a), APDs alternate in a repeating long-short (L-S) pattern, and after (b) electrical pacing control is applied at pacing site ($\boldsymbol{P}$), normal (N) APDs that are closed to $\boldsymbol{P}$ are restored, while (c) illustrates the restoration of normal APDs along the cable when electrical and mechanical perturbation controls are applied respectively at $\boldsymbol{P}$ and over localized region under control (3.25–5 cm from $\boldsymbol{P}$).

Fig. 8(d)]. It has to be noted that when the control signal is applied, I_{sac} is defined as an inward current, as discussed in Sec. III.

The presence of electrical alternans induces, through the mechanism of the so-called excitation-contraction coupling, an alternation in the heart muscle contractile activity; see Fig. 9.

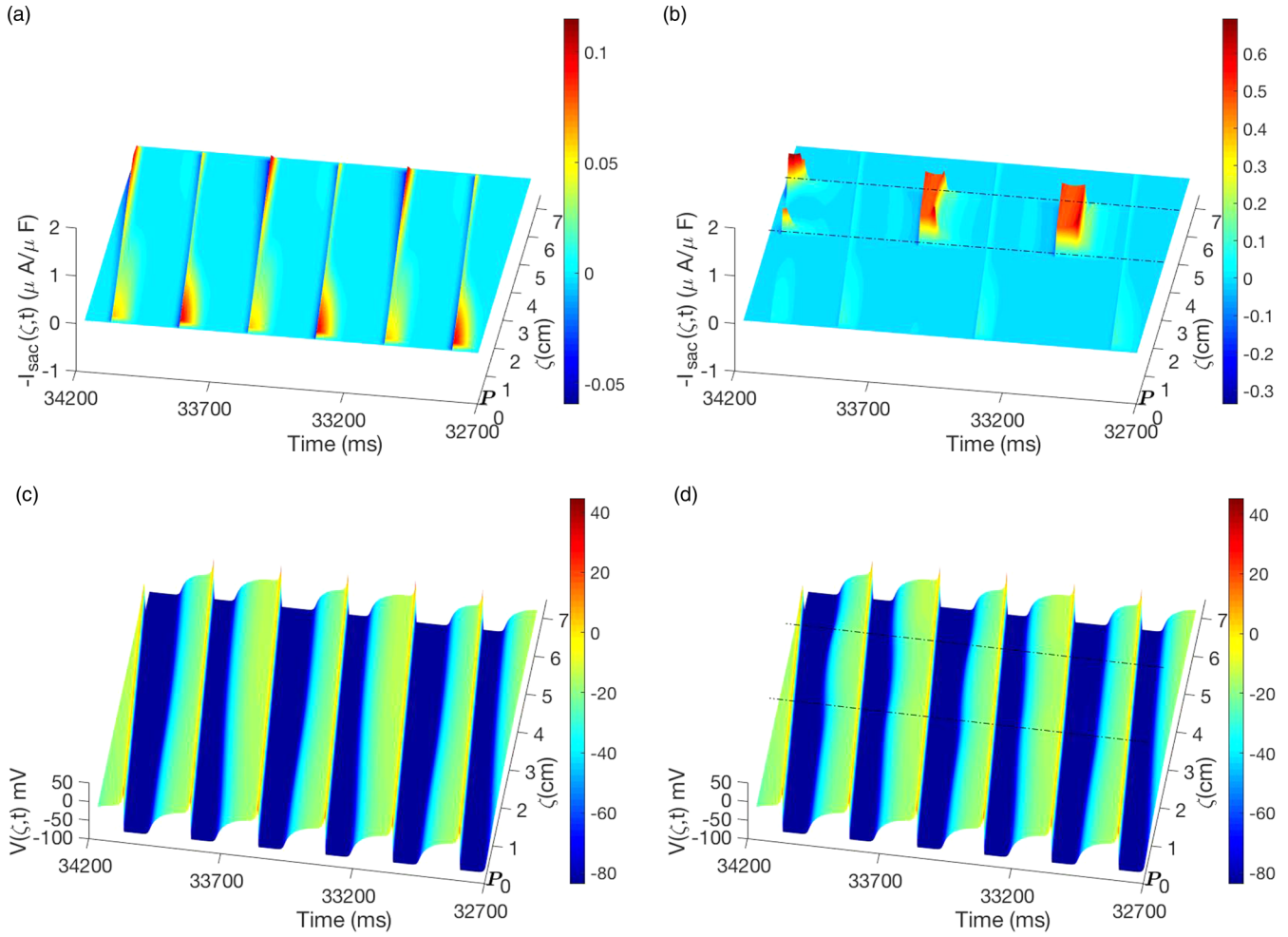

FIG. 8. (a),(c) Time evolution of stretch-activated current (I_{sac}) and membrane potential for model 1, respectively, when only the electrical control is applied, and after (b),(d) the mechanical perturbation control is also applied, at $t = 33\,000$ ms, over localized region under control (3.25–5 cm from $\boldsymbol{P}$). As seen in this figure, the largest changes in I_{sac} (b) with respect to I_{sac} (a), occur in the region (the region between the two dash-dot lines) where mechanical control is applied.

The amplitude of tension alternates [Fig. 9(b)] when the APD alternates [Fig. 9(a)]

As shown in Fig. 10, the error signal decreases from around 20 ms when control is turned on to less than 3 ms at steady state, and the percentage variation in the magnitude of T_a perturbation, where T_a perturbation occurs as a result of $[Ca^{2+}]_{Trpn}$ perturbation, varies from around 10% when control is turned on, to less than 2% at steady state (see Fig. 11). Note that, in real time experiment, perturbing $[Ca^{2+}]_{Trpn}$ by an amount equal to $\beta_1 e_{1n}(\xi)$, as described in Eq. (14), can be difficult to realize, since measurements of the $[Ca^{2+}]_{Trpn}$concentration may not be readily available, and therefore other means such as magnitude of applied force can be used to reconstruct the amount of concentration of $[Ca^{2+}]_{Trpn}$ that needs to be applied. For example, massaging cardiac tissue can perturb $[Ca^{2+}]_{Trpn}$ (change its magnitude) since mechanical perturbation modifies $[Ca^{2+}]_i$ [32], which in its turn modifies the $[Ca^{2+}]_{Trpn}$ [Eq. (11)].

In summary, the control signal alters the tissue's transmembrane potential when mechanical perturbation is applied, in which changes in T_a affect the mechanical deformation term [displacement variable u in the elastic equation (4)], which then affects the transmembrane potential [Eq. (7)], through the conductivity tensor and stretch-activated current [Eq. (5)]. Perturbing MEF alter the tissue's electric wave profile, and consequently the APD. Thus, the control of alternans in cardiac tissues of relevant size can be achieved by the manipulation of the electrical APD using a model based on the mechanical and electrophysiological properties of cardiac tissue.

B. Model 2: Using FOX and NHS models

FOX and NHS models are used in the second electromechanical model to represent electrophysiological properties and active tension generation respectively. The resting potential for the Fox [17] model is about $V_r = -94.7$ mV, and the gains $\gamma = 0.19$, $\beta_1 = -7.4 \times 10^{-4}$ are chosen in model 2.

The alternans is induced by pacing the first ten cells from $\boldsymbol{P}$ of the cable, at $\tau = 300$ ms, until a steady-state APD is reached, and is gradually decreased τ from 300 to $\tau^* = 192$ ms. The pacing period was shortened in steps of 5 ms for $\tau >$ 200 ms and in steps of 1 ms for $\tau < 200$ ms. As shown in

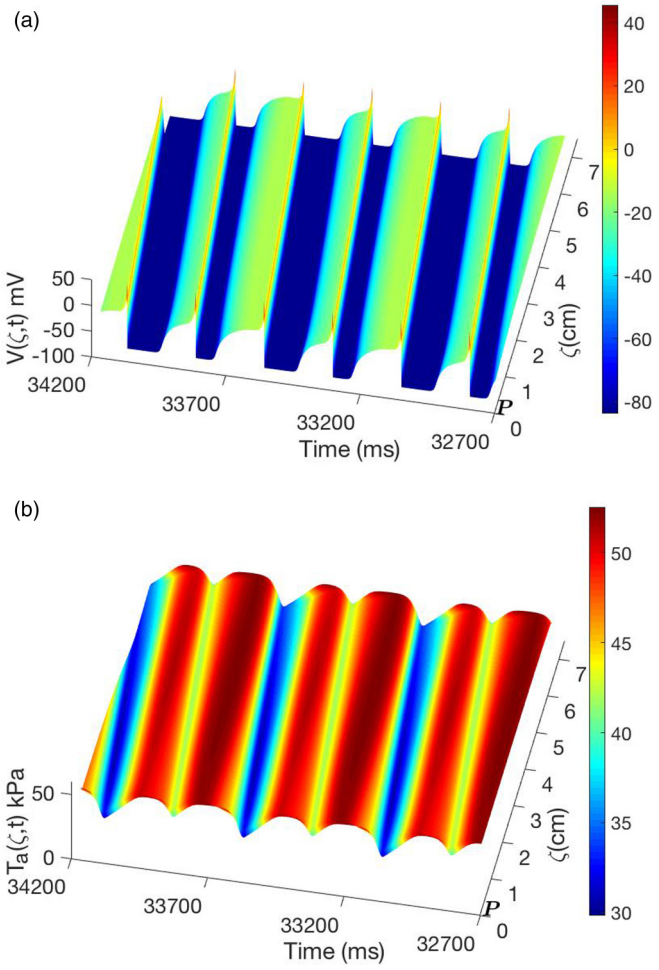

FIG. 9. Time evolution of transmembrane potential variable (a), and active tension variable (b) for model 1 in the presence of alternans. As seen above, the alternation in the APDs induces an alternation in the amplitude of tension through the mechanism of the so-called excitation-contraction coupling.

Fig. 12, the amplitude of alternans grows [Fig. 12(a)] when no control is applied, and when the control action is applied at $t = 25\,000$ ms, over a localized region under control (3.25–5 cm), it successfully suppresses alternans [Fig. 12(c)]. The controller acts after the electrical boundary feedback controller stabilizes a small area (around 1 cm) from $\boldsymbol{P}$ [Fig. 12(b)]. As can be seen in [Fig. 12(b)], $|a_n(\zeta,t)|$ exhibits ripples at the pacing boundary before a steady state is reached, which is then transmitted along the cable. This is due to the pacing period of the dynamic feedback control [Eq. (12)] which varies over many different values depending upon the difference between the last two APDs recorded. The range of variation can be large, especially at the early stages after the control is applied, but when γ [the feedback gain in Eq. (12)] is better tuned, while satisfying the stability requirement [10], the oscillations decay faster. Also, in this model is demonstrated the need to combine the boundary pacing with the spatially distributed mechanical perturbation to successfully suppress alternans.

Similarly to the numerical results for I_{sac} presented in model 1 (see Fig. 8), the largest changes in I_{sac} for model 2, after the mechanical control is applied [Fig.13(b)], with respect to

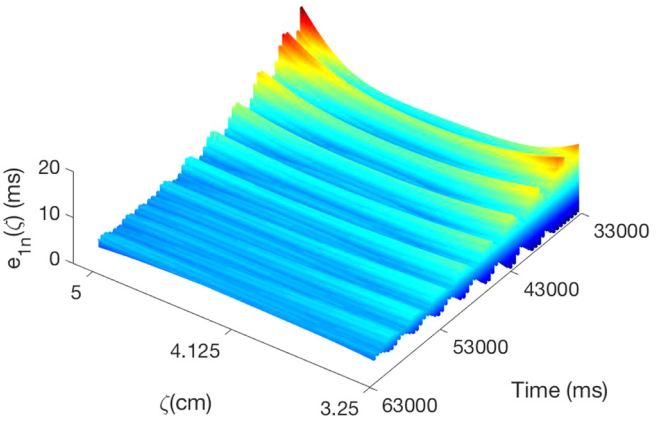

FIG. 10. Time evolution of error signal (e_{1n}), defined in Eq. (14), for model 1, when a spatially distributed mechanical control is applied over localized region under control (3.25–5 cm).

I_{sac}, when only the electrical control is applied [Fig. 13(a)], occur in the region under control. As can be seen in this figure, when mechanical control is turned on at $t = 25\,000$ ms, the magnitude of I_{sac} increases in the region under control for the odd and even beats, which differs from the I_{sac} given in model 1, where the magnitude of I_{sac} increases only for the odd beats. This is because, although the APDs of the even beats remain longer than APDs of the odd beats in the region under control in model 2, they are shorter than $\mathrm{APD}_{\mathrm{ref}}(\tau^*)$.

VI. SUMMARY AND FUTURE WORKS

The development of methods to suppress cardiac alternans has important clinical implications, due to the finding that TWA often precedes lethal arrhythmias, and is a risk factor for SCD. We introduce a theoretical framework of 2D iterative maps that describe the cardiac excitation-contraction coupling. To this end, the stretch-activated current through the stretch-activated ion channels that mediate MEF is approximated in terms of the membrane voltage and the active tension. This allows us to study the effects of the mechanical perturbation algorithm on the dynamics of a developed map model that couples the membrane voltage and active tension at the cellular level. A stability analysis of the system of coupled maps is performed by incorporating a discrete form of the control algorithm. We show that when the mechanical control is turned on, both the stability of APD dynamics and $V \rightarrow T_a$ coupling are affected. That is, the mechanical controller gain affects the eigenvalues of the Jacobian matrix of the system, and thus its stability. Therefore, with an appropriate choice of the gain, the system can be stabilized, and the alternans is suppressed.

The effectiveness of the mechanical perturbation algorithm is verified by employing a model of cardiac electromechanics. Two detailed ionic models of cardiac cell electrophysiology, namely the Luo-Rudy 1 and Fox models, are used, and passive mechanical properties of cardiac muscle are described using the Mooney-Rivlin passive elasticity model. Active tension that couples the cardiac mechanics with excitation is generated using a smooth variant of the Nash-Panfilov model and the Niederer-Hunter-Smith model. The control algorithm is demonstrated to successfully suppress alternans in a 1D cable

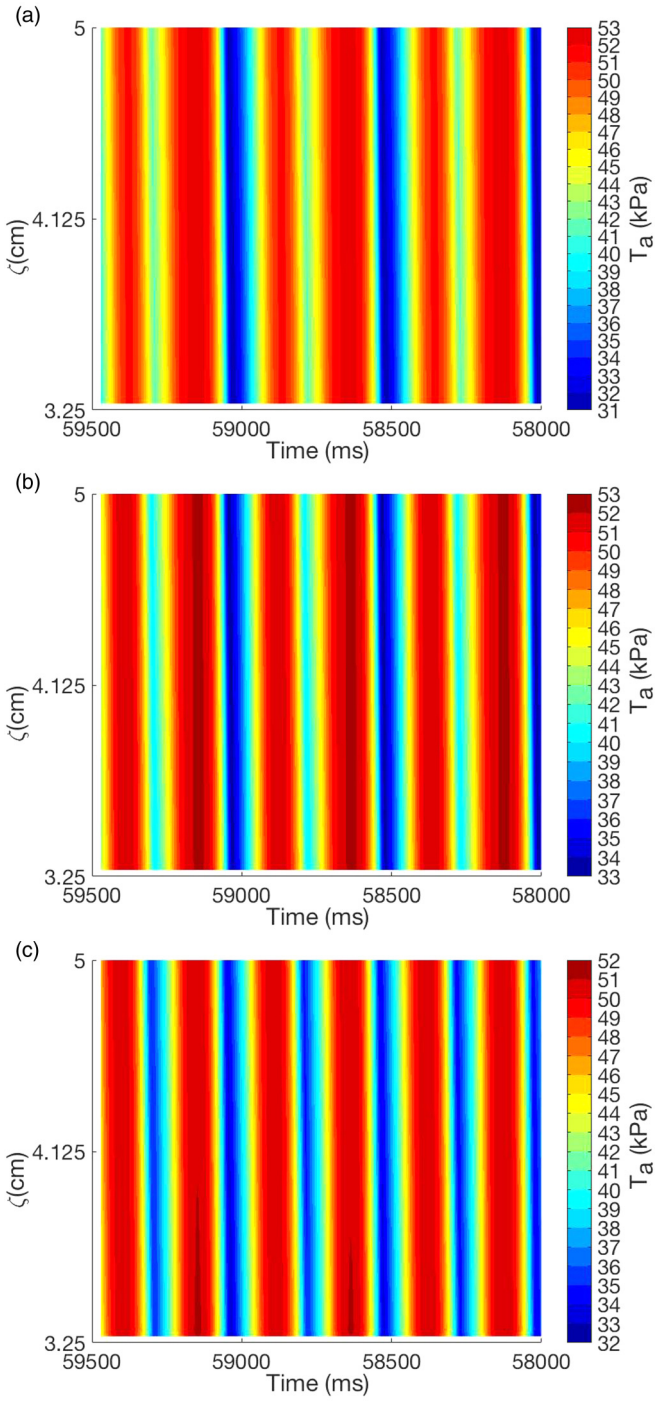

FIG. 11. Time evolution of active tension variable (T_a) [Eq. (9)] in localized region under control (3.25–5 cm) for model 1 when no control is applied (a), while (b) illustrates T_a evolution when only electrical pacing control is applied at pacing site when $\tau^* = 255$ ms is reached, and (c) illustrates the T_a evolution when electrical pacing control and spatially distributed mechanical perturbation control after the control is turned on at $t = 33\,000$ ms over localized region under control.

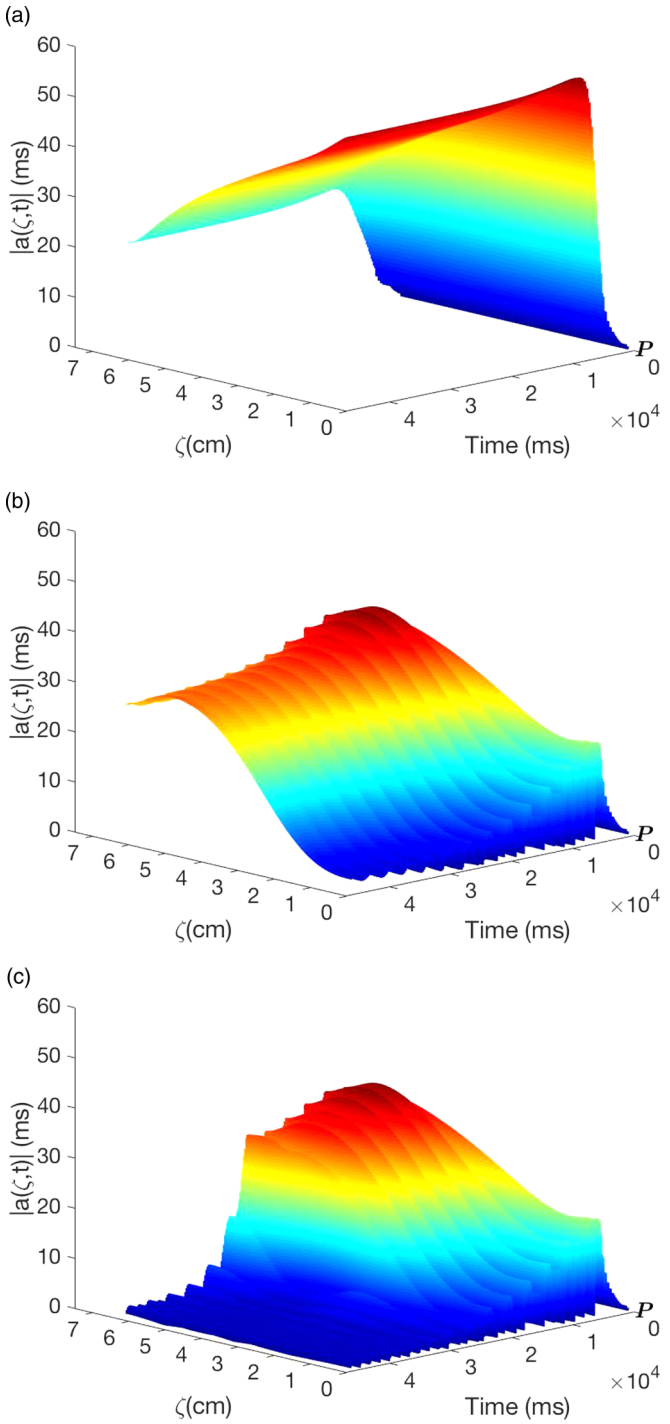

FIG. 12. Magnitude of the amplitude of alternans for model 2 when a 6.25-cm cable of cardiac cells, the first ten cells to ***P***, is paced at 192 ms, starting with period =300 ms, and decreased gradually to period =192 ms. The amplitude of alternans grows, shown in (a), when no control is applied, while (b) illustrates the alternans suppression by electrical pacing control applied at ***P*** when $\tau^* = 192$ ms is reached, and (c) illustrates the alternans suppression by electrical pacing control and spatially distributed mechanical perturbation control when the control action is applied at $t = 25\,000$ ms over localized region under control (3.25–5 cm from ***P***).

of cardiac cells using numerical simulations. If the mechanical perturbation algorithm is incorporated into a mechanical-based device that can be equipped with a mechanical patch, such as [33], alternans rhythms can be suppressed before they become fatal rhythm disorders.

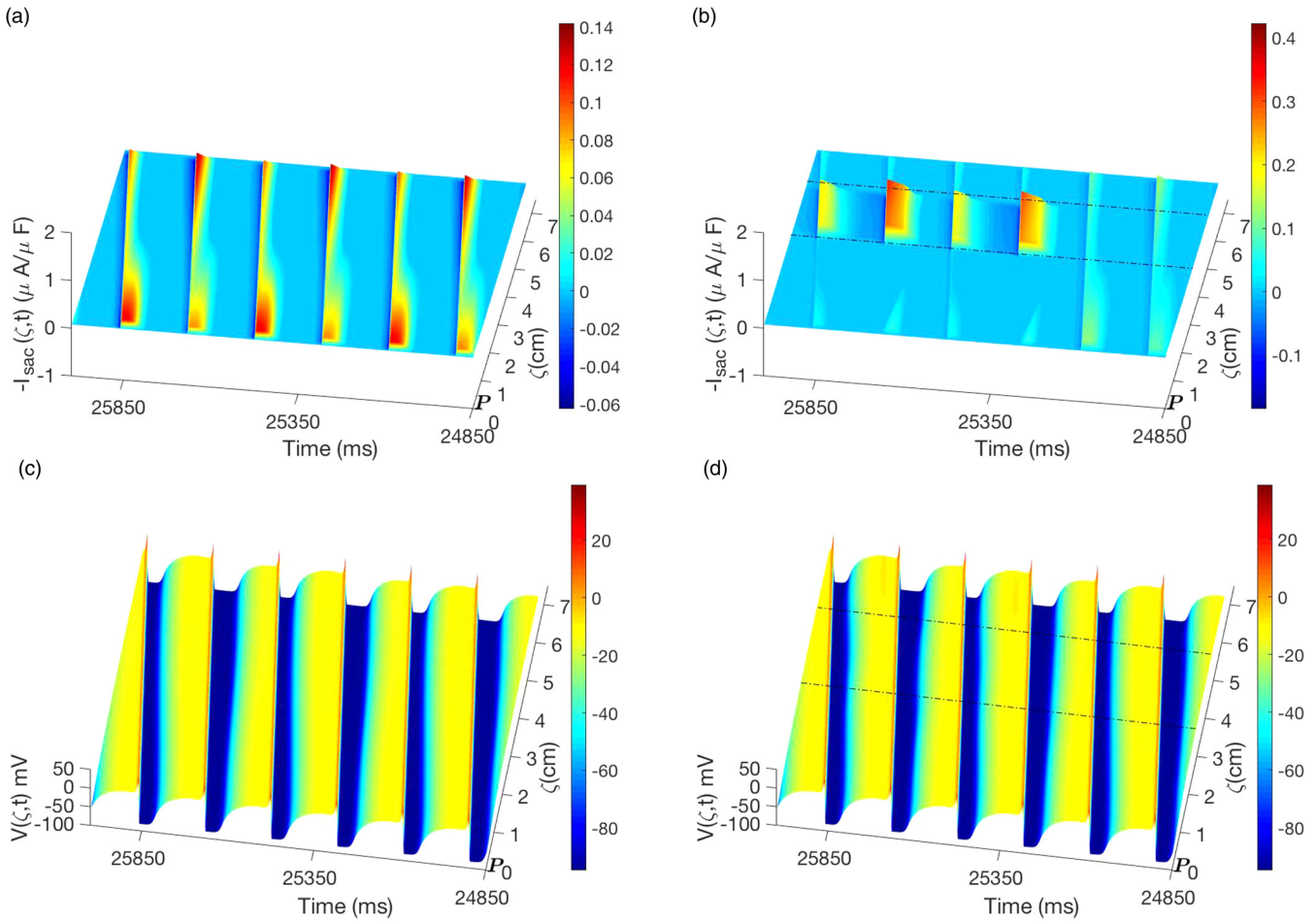

FIG. 13. (a),(c) Time evolution of stretch-activated current (I_{sac}) and membrane potential for model 2, respectively, when only the electrical control is applied, and after (b),(d) the mechanical perturbation control is also applied, at $t = 25\,000$ ms, over localized region under control (3.25–5 cm from $\boldsymbol{P}$). As seen in this figure, the largest changes in I_{sac} (b) with respect to I_{sac} (a) occur in the region (the region between the two dash-dot lines) where mechanical control is applied.

When I_{sac} is applied over a localized region of tissue (chosen by trial and error in our experiments), the spatially distributed mechanical perturbation algorithm successfully suppresses alternans along the tissue. The remaining questions are what is the minimum mechanical patch size necessary and where should the patch be positioned to control alternans? These questions will be addressed in future studies. In addition, tissue anisotropy and fiber orientation will be taken into account when higher-dimensional computational heart models are considered. These factors will affect the distribution of fiber stretch along the tissue, and consequently the magnitude of I_{sac}, which depends on the amount of stretch generated. We expect the size and position of the adhesive patch will influence the magnitude of the mechanical perturbation applied. The majority of studies have neglected the time-dependent inertial term in the equations governing cardiac mechanics (see [34] for a demonstration), therefore, in this work, the inertia term was neglected. But recently [35], it has been shown that the deformations due to inertia may alter the dynamics of excitation waves via the MEF, therefore, this term may be incorporated in future studies.

ACKNOWLEDGMENTS

The authors thank the Natural Science and Engineering Research Council of Canada (NSERC) for financial support. Y.B. thanks the American University of Sharjah for granting a Faculty Research Grant–Travel Grant.

APPENDIX A: APPROXIMATION OF THE EXTENSION RATIO

In one dimension, the extension ratio in the direction of the fiber is calculated from the soft tissue mechanics model, and is given by [6,24]

$$\lambda = \sqrt{C_{11}} = F(X) = 1 + \frac{\partial u(X)}{\partial X}. \tag{A1}$$

If we assume that the maximal stretch of cells, from the resting position, is 5%, we may approximate the inverse of $F(X)$ as

$$F(X)^{-1} = \left(1 + \frac{\partial u(X)}{\partial X}\right)^{-1} \approx 1 - \frac{\partial u(X)}{\partial X}. \tag{A2}$$

The elastic equation (4) can be rewritten as

$$\tilde{c}\,\frac{\partial\left(1+\frac{\partial u(X)}{\partial X}\right)}{\partial X}+\frac{\partial}{\partial X}\left(\frac{T_a(X)}{1+\frac{\partial u(X)}{\partial X}}\right)=0. \tag{A3}$$

By integrating Eq. (A3), we obtain

$$\tilde{c}\left(1+\frac{\partial u(X)}{\partial X}\right)+\frac{T_a(X)}{1+\frac{\partial u(X)}{\partial X}}=C. \tag{A4}$$

The integration constant C is determined by applying boundary conditions. Since a 1D cable fixed at both ends is considered, and thus $\partial u(X)/\partial X = 0[F(X) = 1]$ at the boundaries, we have $C = T_b + \tilde{c}$, where T_b is the active tension at the boundary, which satisfies the following condition:

$$\int_0^L F(X)dX = L. \tag{A5}$$

Replacing C and the approximation of $F(X)^{-1}$ [Eq. (A2)] by their values in Eq. (A4) and solving for $\partial u(X)/\partial X$, we obtain

$$\frac{\partial u(X)}{\partial X}\approx\frac{T_b-T_a(X)}{\tilde{c}-T_a(X)}. \tag{A6}$$

Replacing $\partial u(X)/\partial X$ by its value in Eq. (A1), we obtain

$$F(X)\approx 1+\frac{T_b-T_a(X)}{\tilde{c}-T_a(X)},$$
$$\text{with } T_b\approx\frac{\int_0^L\frac{T_a(X)}{\tilde{c}-T_a(X)}dX}{\int_0^L\frac{1}{\tilde{c}-T_a(X)}dX}, \tag{A7}$$

where T_b is determined by replacing $F(X)$ [Eq. (A7)] by its value in Eq. (A5). Therefore, when $1 < \lambda <= 1.05$, an approximation of λ, given in Eqs. (A1) and (A7), is directly related to T_a, and thus I_{sac}, which is not zero only when the cell is stretched (i.e., when $\lambda > 1$), becomes a function of V and T_a. If we assume that the maximal stretch is 10% (i.e., $\lambda <= 1.1$), the same approximation of λ [Eqs. (A1) and (A7)] can be used to calculate I_{sac}, since the maximum error calculated in the case of model 2, between the exact instantaneous stretch, found by solving the elastic equation (4), and the approximate stretch obtained from Eq. (A7), during one cycle, is less than 1%. This work is not concerned with the complex dynamics of either V or T_a at the cellular level, which would require a more rigorous computation of I_{sac}.

APPENDIX B: JACOBIAN OF THE 2D MAP

The heart beat-to-beat dynamics using a 2D discrete map between the APD and the ATD is given as

$$\begin{aligned}\text{APD}_n &= F_1(\text{APD}_{n-1},\text{ATD}_n),\\ \text{ATD}_n &= F_2(\text{APD}_{n-1},\text{ATD}_{n-1}).\end{aligned} \tag{B1}$$

Let $F=[F_1,F_2]^T$, and $X_n=[x_n,y_n]^T=[\text{APD}_n,\text{ATD}_n]^T$; then the map [Eq. (B1)] can be written in the matrix form as

$$X_n = F(X_{n-1}). \tag{B2}$$

At the period-1 fixed point $X_*=[\text{APD}_*,\text{ATD}_*]^T$, we have $X_n = F(X_{n-1}) = X_{n-1} = X_* = F(X_*)$. Let $\delta X_n = [\delta\text{APD}_{n-1},\delta\text{ATD}_{n-1}]^T$ be a small displacement from the point X_*; we can then write

$$X_* + \delta X_n = F(X_* + \delta X_{n-1}). \tag{B3}$$

Using the Taylor expansion, we can linearize the system of coupled maps around the point X_* as follows:

$$F(X_* + \delta X_{n-1}) \approx F(X_*) + J\ \delta X_{n-1}, \tag{B4}$$

where

$$J=\begin{bmatrix}\frac{\partial F_1}{\partial x_{n-1}} & \frac{\partial F_1}{\partial y_{n-1}}\\ \frac{\partial F_2}{\partial x_{n-1}} & \frac{\partial F_2}{\partial y_{n-1}}\end{bmatrix}, \tag{B5}$$

where $J_{11}=\frac{\partial F_1}{\partial \text{APD}_{n-1}}$, $J_{12}=\frac{\partial F_1}{\partial \text{ATD}_{n-1}}$, $J_{21}=\frac{\partial F_2}{\partial \text{APD}_{n-1}}$, and $J_{22}=\frac{\partial F_2}{\partial \text{ATD}_{n-1}}$ are the elements of the Jacobian J evaluated at the fixed point $(\text{APD}_*,\text{ATD}_*)$ of the map. From Eqs. (B3) and (B4) we can write

$$\delta X_n \approx J\ \delta X_{n-1}. \tag{B6}$$

[1] G. R. Mines, J. Physiol. **46**, 349 (1913).
[2] L. Makarov and V. Komoliatova, ANN Noninvas Electro. **15**, 138 (2010).
[3] S. M. Narayan, J. Am. Coll. Cardiol. **49**, 347 (2007).
[4] D. S. Rosenbaum, L. E. Jackson, J. M. Smith, H. Garan, J. N. Ruskin, and R. J. Cohen, New Engl. J. Med. **330**, 235 (1994).
[5] A. Gizzi, E. M. Cherry, R. F. Gilmour Jr., S. Luther, S. Filippi, and F. H. Fenton, Front. Physiol. **4**, 71 (2013).
[6] A. Hazim, Y. Belhamadia, and S. Dubljevic, Comput. Biol. Med. **63**, 108 (2015).
[7] J. B. Nolasco and R. W. Dahlen, J. Appl. Physiol. **25**, 191 (1968).
[8] M. R. Guevara, G. Ward, A. Shrier, and L. Glass, IEEE Comp. Cardiol. **562**, 167 (1984).
[9] K. Hall, D. J. Christini, M. Tremblay, J. J. Collins, L. Glass, and J. Billette, Phys. Rev. Lett. **78**, 4518 (1997).
[10] B. Echebarria and A. Karma, Chaos **12**, 923 (2002).
[11] Y. Shiferaw, D. Sato, and A. Karma, Phys. Rev. E **71**, 021903 (2005).
[12] Y. Shiferaw and A. Karma, Proc. Natl. Acad. Sci. U.S.A. **103**, 5670 (2006).
[13] Z. Qu, Y. Shiferaw, and J. N. Weiss, Phys. Rev. E **75**, 011927 (2007).
[14] D. Sato, Y. Shiferaw, A. Garfinkel, J. N. Weiss, Z. Qu, and A. Karma, Circ. Res. **99**, 520 (2006).
[15] F. Yapari, D. Deshpande, Y. Belhamadia, and S. Dubljevic, Phys. Rev. E **90**, 012706 (2014).
[16] C. Luo and Y. Rudy, Circ. Res. **68**, 1501 (1991).
[17] J. J. Fox, J. L. McHarg, and R. F. Gilmour Jr., Am. J. Physiol. Heart Circ. Physiol. **282**, H516 (2002).
[18] M. P. Nash and A. V. Panfilov, Prog. Biophys. Mol. Biol. **85**, 501 (2004).
[19] E. Kuhl and S. Göktepe, Comput. Mech. **45**, 227 (2010).

[20] S. A. Niederer, P. J. Hunter, and N. P. Smith, Biophys. J. **90**, 1697 (2006).
[21] D. Ambrosi and S. Pezzuto, J. Elast. **107**, 199 (2012).
[22] P. Kohl, P. Hunter, and D. Noble, Prog. Biophys. Mol. Biol. **71**, 91 (1999).
[23] F. J. Vetter and A. D. McCulloch, Ann. Biomed. Eng. **29**, 414 (2001).
[24] R. H. Keldermann, M. P. Nash, H. Gelderblom, V. Y. Wang, and A. V. Panfilov, Am. J. Physiol. Heart Circ. Physiol. **299**, H134 (2010).
[25] J. Keener and J. Sneyd, *Mathematical Physiology* (Springer-Verlag, New York, 1998).
[26] C. Cherubinia, S. Filippia, A. Gizzia, and R. Ruiz-Baierc, J. Theor. Biol. **430**, 221 (2017).
[27] H. Dal, S. Göktepe, M. Kaliske, and E. Kuhl, Comput. Meth. Appl. Mech. Eng. **253**, 323 (2013).
[28] D. J. Christini, M. L. Riccio, C. A. Culianu, J. J. Fox, A. Karma, and R. F. Gilmour, Phys. Rev. Lett. **96**, 104101 (2006).
[29] S. Dubljevic, S. F. Lin, and P. D. Christofides, Comput. Chem. Eng. **32**, 2086 (2008).
[30] R. H. Keldermann, M. P. Nash, and A. V. Panfilov, Physica D (Amsterdam) **238**, 1000 (2009).
[31] S. Rush and H. Larsen, IEEE Trans. Biomed. Eng. **BME-25**, 389 (1978).
[32] E. R. Pfeiffer, J. R. Tangney, J. H. Omens, and A. D. McCulloch, J. Biomech. Eng. **136**, 021007 (2014).
[33] L. Xu, S. R. Gutbrod, A. P. Bonifas, Y. Su, M. S. Sulkin, N. Lu, H.-J. Chung, K.-I. Jang, Z. Liu, M. Ying, C. Lu, R. C. Webb, J.-S. Kim, J. I. Laughner, H. Cheng, Y. Liu, A. Ameen, J.-W. Jeong, G.-T. Kim, Y. Huang, I. R. Efimov, and J. A. Rogers, Nat. Commun. **5**, 3329 (2014).
[34] J. P. Whiteley, M. J. Bishop, and D. J. Gavaghan, Bull. Math. Biol. **69**, 2199 (2007).
[35] F. Sahli Costabal, F. A. Concha, D. E. Hurtado, and E. Kuhl, Comput. Meth. Appl. Mech. Eng. **320**, 352 (2017).